Journal of Alloys and Compounds 512 (2012) 105–114

Contents lists available at SciVerse ScienceDirect

Journal of Alloys and Compounds

journal homepage: www.elsevier.com/locate/jallcom

Microstructure, mechanical, EPR and optical properties of lithium disilicate glasses and glass–ceramics doped with Mn^{2+} ions

A.R. Molla[a,*], R.P.S. Chakradhar[b], C.R. Kesavulu[c], J.L. Rao[c], S.K. Biswas[d]

[a] Glass Science and Technology Section, Glass Division, CSIR-Central Glass and Ceramic Research Institute, Kolkata 700032, India
[b] CSIR-National Aerospace Laboratorie(s), Bangalore 560017, India
[c] Department of Physics, S.V. University, Tirupati 517502, India
[d] Non-oxide Ceramics and Composite Division, CSIR-Central Glass and Ceramic Research Institute, Kolkata 700032, India

ARTICLE INFO

Article history:
Received 25 April 2011
Received in revised form
12 September 2011
Accepted 12 September 2011
Available online 29 September 2011

Keywords:
Glass
Glass–ceramics
Microstructure
EPR
Optical
Mechanical properties

ABSTRACT

The microstructure, mechanical, EPR and optical properties of transparent MnO_2 doped lithium disilicate (LDS) glass–ceramics prepared by melt quenching and controlled crystallization, have been studied. The microstructure of the glass–ceramics has been characterized using FE-SEM, TEM, FT-IR and XRD techniques. FE-SEM micrographs show elongated, highly interlocked, dense (~80 vol.%) nanocrystals of LDS with an average size ~100 nm. XRD and FT-IR studies reveal that the only crystalline phase formed after heat-treatment at 700 °C for 1 h is LDS. A good combination of average microhardness ~5.6 GPa, high fracture toughness ~2.8 MPa m$^{1/2}$, 3-point flexural strength ~250 MPa and moderate elastic modulus 65 GPa has been obtained. The EPR spectra of both LDS glasses and glass–ceramics exhibit resonance signals with effective g values at $g = 4.73$, $g = 4.10$, $g = 3.3$, and $g = 1.98$. The resonance signal at $g = 1.98$ is found to be more intense than the other signals and exhibits hyperfine structure at lower concentration of manganese. From the observed spectrum, the spin-Hamiltonian parameters have been evaluated. In glass samples the optical absorption spectrum exhibits a broad band around ~20,320 cm^{-1} which has been assigned to the transition $^6A_{1g}(S) \rightarrow {}^4A_{1g}(G)\,{}^4E_g(G)$-of Mn^{2+} ions. The cerammed samples upon 394 nm excitation emit a green luminescence (565 nm, $^4T_{1g} \rightarrow {}^6A_{1g}(G)$ transition of Mn^{2+} ions), and a weak red emission (710 nm). From the ultraviolet absorption edges, the optical bandgap energies (E_{opt}) were evaluated and are discussed.

1. Introduction

Lithium disilicate (LDS) glass–ceramics (GC) demonstrating high strength [1] have been produced by various techniques such as controlled nucleation and crystallization of the base glasses through heat treatment [2] and sintering technology [3]. Melting together with heat-treatment offers very good reproducibility compared with the alternative method based on powder processing and sintering commonly used in polycrystalline ceramics, which is prone to microstructural inhomogeneity [4]. Owing to its remarkable mechanical properties, this material is widely used for various biomedical applications [5,3] and more recently as transparent armours [6]. Further, chemical strengthening by ion exchange treatments can increase the strength of lithium disilicate glass–ceramics considerably so that the material can be used for highly stressed applications, such as posterior crowns or inlay-retained bridges, with higher mechanical reliability [7]. Such glass–ceramics appear to be ideal for advanced armour applications due to their low density, relatively high transparency and fracture strength, and their thermal and chemical stability [4]. Indeed the chemical durability of both the LDS glasses and glass–ceramics is reported as excellent [8]. Cheng et al. [9] studied properties of LDS GC and found useful as an anodic bonding materials. The influence of nucleating agents such as ZrO_2 and P_2O_5 on the crystallization and properties of LDS glass–ceramics has been reported by various researchers [2,10–12]. The effect of heat-treatment conditions on thermal expansion, phase distribution and mechanical properties were examined by Bengisu and Brow [13]. Various researchers have investigated the crystallization kinetics [14–16] of LDS glass–ceramics and also studied metastable phase formation [14,15,17]. The structure of $Li_2O{\cdot}2SiO_2$ (LS2) glass was investigated by Fuss et al. [18,19] as a function of pressure and temperature, respectively, using XRD, TEM,IR, Raman and NMR spectroscopy. The crystallization mechanism of a high-strength lithium disilicate glass–ceramic has been examined on the basis of quantitative ^{29}Si magic angle spinning (MAS) and $^{29}Si\{^7Li\}$ rotational echo double resonance (REDOR) NMR spectroscopy by Bischoff et al. [20]. They have reported that in this system crystallization occurs in two stages: near 650 °C crystalline Li_2SiO_3 forms and upon further annealing of this glass–ceramic

---

[*] Corresponding author. Tel.: +91 33 24733469; fax: +91 33 24730957.
E-mail addresses: atiar@cgcri.res.in, atiariitk@gmail.com (A.R. Molla).

0925-8388/$ – see front matter © 2011 Elsevier B.V. All rights reserved.
doi:10.1016/j.jallcom.2011.09.031

Table 1
Composition (wt.%) of glasses studied in the present work.

Oxides	LDS1G	LDS2G	LDS3G	LDS4G
SiO_2	70.64	70.64	70.64	70.64
K_2O	3.09	3.09	3.09	3.09
Li_2O	14.68	14.68	14.68	14.68
Al_2O_3	3.38	3.38	3.38	3.38
P_2O_5	3.21	3.21	3.21	3.21
ZrO_2	3.00	3.00	3.00	3.00
CeO_2	1.88	1.88	1.88	1.88
MnO_2	0.12	1.0	3.0	5.0

to 850 °C the crystalline Li_2SiO_3 phase reacts with the softened residual glass matrix, resulting in the crystallization of $Li_2Si_2O_5$ (LDS). Höland et al. [3] studied the microstructure and properties of different dental glass–ceramics and reported a fracture toughness value for LDS glass–ceramics of 3.3 ± 0.3 MPa $m^{1/2}$. Very recently, mechanical and chemical properties of Zr and P-doped lithium disilicate glass–ceramics for dental restorations have been studied by Khalkhali et al. [21] and reported that the P-doped glass ceramic exhibited the optimum mechanical and chemical properties (i.e. $m = 5$, $\sigma_f = 181 \pm 15$ MPa, $K_{IC} = 1.94 \pm 0.19$ MPa $m^{1/2}$, $H_v = 3.7 \pm 1.1$ GPa, chemical solubility = 53 ± 9 μg/cm^2). Goharian et al. [22] have reported 3-point flexural strength of 280 MPa for a LDS glass–ceramics sample. However, studies of photoluminescence, optical properties, electron paramagnetic resonance (EPR) of lithium disilicate glass–ceramics and their correlation with its structural and mechanical properties have not been reported so far.

In the present study, LDS glass-ceramics have been prepared by melt-quenching followed by controlled heat-treatment. The samples have been characterized by X-ray diffraction (XRD), field-emission scanning electron microscopy (FE-SEM), transmission electron microscopy (TEM) and Fourier transform infrared spectroscopy (FT-IR) techniques. Photoluminescence (PL) and electron paramagnetic resonance (EPR) studies have also been carried out on the prepared glasses and glass ceramics. Electron paramagnetic resonance spectroscopy (EPR) will provide useful information about the oxidation states, types of coordination and geometry of the ligand sites. The static and dynamic properties are affected by their environments as the 3d electrons occupy orbitals extending to the outside of the ions. Upon ceramming, the local environment of the transition metal ion incorporated into the glass leads to ligand field changes which may be reflected in the optical absorption and EPR spectra.

2. Experimental

Four glasses as per the composition presented in Table 1 were prepared by a conventional melt-quench technique from high-purity chemicals: Quartz (SiO_2) (99.8%, Sipur A1 Bremtheler Quartzitwerk, Usingen, Germany), aluminum oxide hydrate [$Al(OH)_3$] (CHP-340S, Sumito Chemical Company, Japan), aluminum orthophosphate ($AlPO_4$) (Chemische Fabrik Budenheim KG, Budenheim, Germany), zirconia (ZrO_2) (Grade TZ-0, TOSOH, Tokyo, Japan), lithium carbonate (Li_2CO_3) (Merck KGaA, Darmstadt, Germany), potassium carbonate (K_2CO_3) (Merck KGaA, Darmstadt, Germany), cerium(IV) oxide (Merck KGaA, Darmstadt, Germany) and manganese(IV) oxide (Merck KGaA, Darmstadt, Germany). The compositions of LDS glass ceramics used for the present study were based on an earlier work reported by Höland et al. [23] with some minor modifications, such as replacement of V_2O_5 with MnO_2. Four concentrations of MnO_2, 0.12, 1.0, 3.0 and 5.0 in wt.% have been used to see the effect of MnO_2 on the properties of LDS GC and the samples are designated as LDS1G, LDS2G, LDS3G and LDS4G, respectively. About 50 g of glass batch was mixed thoroughly in an agate-mortar and was melted in a platinum crucible in an electric furnace at 1550 °C for 2 h in air with intermittent stirring. The glass melt was poured onto a preheated iron mould, followed by annealing at 500 °C for 2 h to remove the internal stresses of the glass, and then slowly cooled down at 1 °C/min to room temperature. The as-prepared glass block was shaped into the desired dimensions by cutting and optically polished to carry out various characterization experiments. These precursor glasses, i.e. LDS1G, LDS2G, LDS3G and LDS4G were heat-treated at 700 °C for 1 h to convert them into glass–ceramics.

Archimedes's principle was employed to determine densities of the glasses and glass–ceramics with water as the immersion liquid on a single pan electrical balance accurate to the nearest 0.00001 g. The error in density measurement is estimated to be ±0.004 g/cm^3. DTA of precursor glass powders were carried out at temperatures up to 1000 °C at the rate of 10 °C/min with a NETZSCH instrument (Model STA 449C, NETZSCH-Gerätebau GmbH, Germany) to determine the glass transition (T_g) and crystallization temperatures. XRD data were recorded using an Xpert-Pro MPD diffractometer (PANalytical, Almelo, The Netherlands) with the anchor scan parameters wavelength Cu Kα = 1.5406 Å at 25 °C, having a source power of 40 kV and 30 mA, in order to identify the crystalline phases developed in the heat-treated glass–ceramics. A high-resolution FE-SEM (Gemini Zeiss Suprat 35 VP model of Carl Zeiss Microimaging GmbH, Berlin, Germany) was used to observe the microstructure of the heat-treated glass–ceramics after etching in HF solution and coating with a thin carbon film. The TEM images of the powdered glass–ceramic samples were obtained from an FEI (Model Tecnai G2 30ST, FEI Company, Hillsboro, OR) instrument. The FT-IR transmittance spectra were plotted using a FT-IR spectrometer (Model 1615, PerkinElmer), in the wavenumber range 400–2000 cm^{-1} at a resolution of ±2 cm^{-1} after 16 scans. The refractive index (RI) of the precursor glass was measured by a Prism Coupler (Model 2010/M, Metricon Corporation, New Jersey, USA) at five different wavelengths of 473, 532, 632.8, 1064 and 1552 nm using appropriate laser sources. Further, these data have been used to estimate RI at other wavelengths employing the Sellemeyer dispersion equation. The resolution of the prism coupler is ±0.0005. The optical absorption spectra were recorded on a PerkinElmer UV–vis spectrophotometer (Model Lambda 20, PerkinElmer Corporation, Waltham, MA, USA) in the wavelength range of 400–1100 nm with an accuracy of ±1%. The band position was measured digitally and the accuracy with which the peaks were measured was ±10 cm^{-1}. The fluorescence spectra were measured to ±0.2 nm with a fluorescence spectrophotometer (Fluorolog 2, Spex) using a 150 W Xe lamp as the excitation source and a photomultiplier tube (PMT) as detector.

The EPR spectra were recorded on an EPR spectrometer (JEOL-FE-1X) operating in the X-band frequency (≈9.200 GHz) with a field modulation frequency of 100 kHz. The magnetic field was scanned from 0 to 500 mT and the microwave power used was 10 mW. A powdered glass sample of 100 mg in a quartz tube was used for EPR measurements. The hardness and indentation fracture toughness properties of the glass ceramic samples were measured by micro-indentation on the polished surface of the samples using a microindentation hardness testing system (Clemex CMT, Canada) equipped with a conical Vicker's indenter at an indent load of 500 g. About 10 indents were taken for each sample using identical loading conditions. The diagonals of the Vickers indents were carefully measured using an optical microscope and subsequently, the hardness was calculated using the standard equation for the Vickers geometry:

$$H_v = 1.8544 \frac{P}{d^2} \tag{1}$$

where H_v is the Vickers hardness number (VHN) in kg/mm^2, P is the normal load in kg, and d is the average diagonal length of the indentation in mm. The following equation proposed by Antis et al. [24] was used for calculation of the fracture toughness (K_{IC}):

$$K_{IC} = \alpha \left(\frac{E}{H}\right)^{0.5} \left(\frac{P}{C^{1.5}}\right) \tag{2}$$

where P is the applied load and C is the mean length of the two radian cracks. E and H are the Young's modulus and hardness of the sample, respectively, measured at the same applied load P at which the K_{IC} of the sample is measured. For Vicker's indenters the α value was taken as 0.016. The elastic modulus and flexural strength were measured using 3-point bending set upon Instron machine. During 3-point flexural tests, the displacement of the bar sample was measured by placing a LVDT (linear variable displacement transducer) adjacent to the tensile surface. From the slope of the linear part of the obtained load displacement curve, the E-modulus was measured. The flexural properties were evaluated using a span length of 40 mm and crosshead speed of 0.5 mm/min at a temperature of 25 °C and relative humidity of 70%.

3. Results and discussion

3.1. Physical and thermal properties

A DTA study is a pre-requisite to determining the heat-treatment conditions needed to convert a glass system into a glass–ceramic with the desired crystalline phases. DTA traces for LDS1G, LDS2G and LDS3G are provided in Fig. 1. No significant differences in the glass transition temperatures (T_g) between the glasses LDS1G (488 °C), LDS2G (488 °C) and LDS3G (487 °C) were observed because the compositional differences in the base glass are small other than minor variations in the MnO_2 dopant content. It has also been observed that there are two exothermic peaks at

Table 2
Certain physical parameters and optical properties of the lithium disilicate glass and glass–ceramic samples studied in the present work.

Sample	Density (g/cc)	n'_F	n_d	n'_C	Abbe number (ν_e)	Dielectric constant (ε)	Reflection loss (R%)
LDS1G	2.428	1.5449	1.5387	1.5331	45.65	2.371	4.52
LDS2G	2.448	1.5488	1.5424	1.5371	46.36	2.385	4.57
LDS3G	2.456	1.5508	1.5449	1.5392	46.97	2.390	4.59
LDS4G	2.478	1.5549	1.5491	1.5427	45.00	2.403	4.65
LDS1GC	2.466	1.5478	1.5422	1.5356	44.44	2.380	4.55
LDS2GC	2.477	1.5512	1.5455	1.5393	45.84	2.393	4.61
LDS3GC	2.501	1.5533	1.5479	1.5416	46.83	2.400	4.64
LDS4GC	2.509	–	–	–	–	–	–

631 °C and 832 °C in the DTA curve of sample LDS1, whereas, in samples LDS2 and LDS3 broad exothermic peaks are noticed at 721 °C and 696 °C, respectively. Similar thermal behaviour was reported by Apel et al. [2] for the LDS glass–ceramics studied by them. The exothermic peak observed at 631 °C in the DTA curve of LDS1 is due to the crystallization of lithium metasilicate (Li_2SiO_3) [2] which is dissolved at higher temperatures to form lithium disilicate ($Li_2Si_2O_5$) at 832 °C. This finding is in good agreement with those of other researchers [2]. Distinct exothermic peaks are not observed at higher temperatures (>700 °C) in the DTA curves of LDS2 and LDS3 possibly due to the overlapping of the crystallization events for formation of lithium metasilicate and lithium disilicate crystals. With an increase in the MnO_2 content in the glasses, their density increases monotonically by a small amount. Table 2 lists the densities of lithium disilicate (LDS) glass and glass–ceramics studied in the present work. The densities of the glass–ceramics were found to be higher than that of their glass counterpart due to the obvious reason that after heat-treatment when glass–ceramic forms, densification takes place. Overall, the densities of these glasses and glass–ceramics are found to be 2.5 g cm^{-3} or less. The density of the lithium disilicate glasses and glass–ceramics are much lower than that of the other ceramics (e.g. density of Al_2O_3 ~ 4.0 g cm^{-3}) or metals (e.g. density of steel ~ 7.85 g cm^{-3}) commonly used for armour applications. This implies that armour with a lower weight per unit area could be designed with LDS GC, while providing the same level of protection in comparison with the conventional armour grade steel and ceramics.

3.2. X-ray diffraction

To make glass-ceramics the precursor glasses LDS1G, LDS2G, LDS3G and LDS4G were subjected to a single stage heat-treatment at 700 °C for 1 h with heating and cooling rates of 2 °C/min. XRD patterns of the heat-treated glass–ceramic samples are shown in Fig. 2. The samples are designated as LDS1GC, LDS2GC, LDS3GC and LDS4GC for four different glass–ceramics with varying concentration of MnO_2. After heat-treatment, all these glass–ceramics were found to be transparent and the major crystalline phase identified in all these glass–ceramics was LDS, the main diffraction peaks corresponding to those reported in the JCPDS file card no. 40-0376. Thus, lithium disilicate is the only crystalline phase in the glass–ceramic. The change in MnO_2 concentrations does not introduce any additional peaks and the intensities of peaks observed are similar for all the compositions, indicating the absence of any Mn-containing crystalline phase. However, further investigations need to be carried out to ascertain the role of Mn ions, if any, in crystallization of lithium disilicate by observing X-ray time structure analyses.

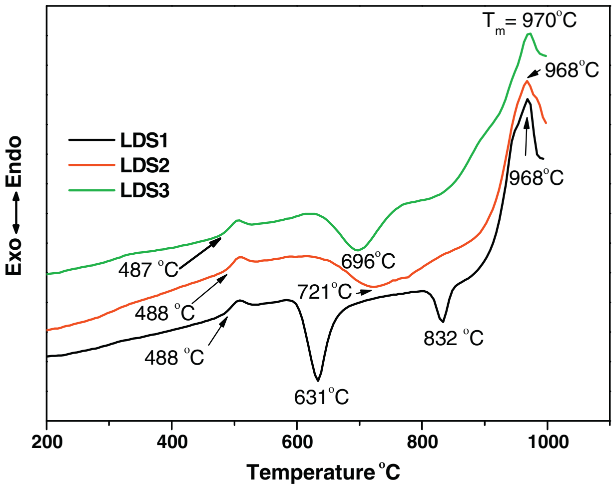

Fig. 1. DTA traces of lithium disilicate glasses.

3.3. FE-SEM and TEM analysis

Field emission scanning electron microscopy (FE-SEM) and transmission electron microscopy (TEM) measurements have been used to investigate the nucleation and crystallization processes. FE-SEM micrographs of lithium disilicate glass–ceramics heat-treated at 700 °C for 1 h are shown in Fig. 3. The glass–ceramics were etched with 10% hydrofluoric acid for 60 s prior to FE-SEM observations. The applied etching procedure resulted in the glassy matrix of the samples dissolving from the surface areas in a few microns, which exposed a layer of crystals on the surface of the glass matrix and imparted a high contrast for the scanning electron microscope investigations. The glass–ceramic displayed a fine microstructure with many lithium disilicate crystals of uniform size homogeneously dispersed in the glass matrix. The crystals are elongated and highly interlocked with each other, which is responsible for the high mechanical strength of the glass-ceramic. The individual crystals are nearly spherical in shape. Critical examination of the elongated crystals formed and the similarity between the dimension of the crystal grains and the diameter of the elongated crystals reveals

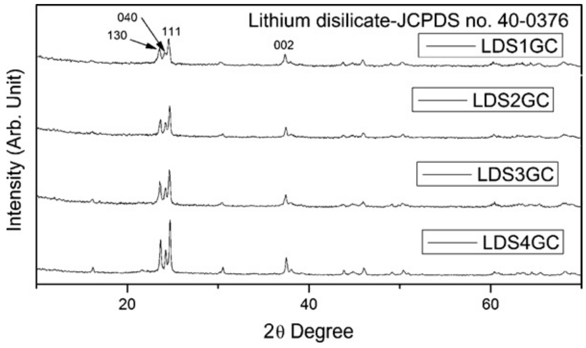

Fig. 2. XRD patterns of lithium disilicate glass–ceramics heat-treated at 700 °C for 1 h.

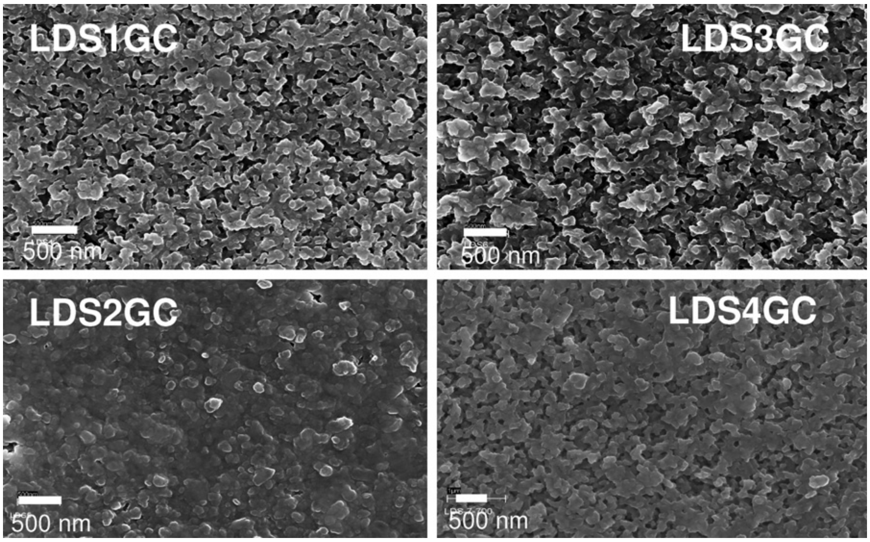

Fig. 3. FE-SEM micrographs of lithium disilicate glass–ceramics heat-treated at 700 °C for 1 h.

that grains are connected side by side epitaxially which leads to the formation of this kind of morphology of elongated crystals of nano-size. The glass–ceramics produced in the present investigation are transparent due to the development of nano-sized crystals. The crystals of average grain size of about 100 nm were measured for all the samples. Similar crystal morphology of lithium disilicate glass–ceramics was reported by previous researchers [23,25]. However, reports show that crystals of rod shaped morphology can be formed in the LDS glass–ceramics if heated for a longer duration at higher temperatures (>800 °C). The content of lithium disilicate in the heat-treated glass–ceramics were 80 ± 5 vol.%, which were determined from the microstructure by adopting stereological technique using grid paper. Because of this dense interlocked morphology of crystals, it shows high mechanical strength. The initiation of the nucleation process in a very homogeneous glass enables growth of this kind. The microstructures of heat-pressed lithium disilicate have been studied by Höland et al. [3] who reported a different microstructure for the LDS glass–ceramics. They reported elongated LDS crystals of 0.5–4 μm length, which is bigger, compared to the crystallite sizes observed in the present investigation (~100 nm). Moreover, they reported crystal volume fractions of 0.7, which is less compared to the presently studied samples (0.8).

Further, TEM observation was carried out to examine the crystallization behaviour of the heat-treated glass–ceramics. The bright field TEM images of LDS1GC, LDS2GC, LDS3GC and LDS4GC glass–ceramics are shown in Fig. 4. The TEM images reveal the presence of nanocrystals of average size 10–50 nm in LDS1GC, LDS2GC, LDS3GC and LDS4GC glass–ceramics. Due to the presence of small crystallites, the LDS glass–ceramics produced in the present investigation are found to be transparent. The details of the optical properties of the LDS glasses and glass–ceramics are discussed in the subsequent sections.

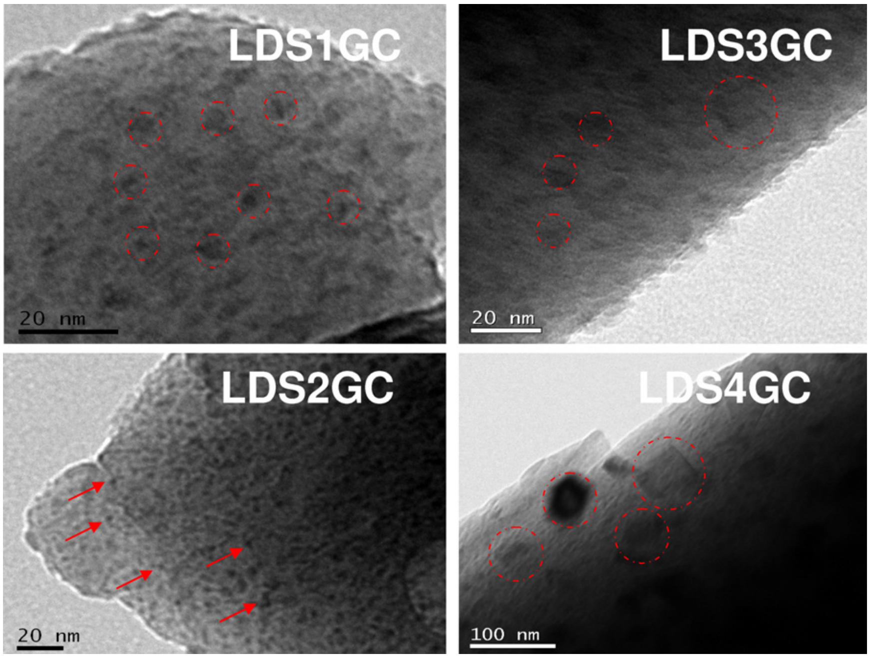

Fig. 4. TEM micrographs of LDS glass–ceramics heat-treated at 700 °C for 1 h.

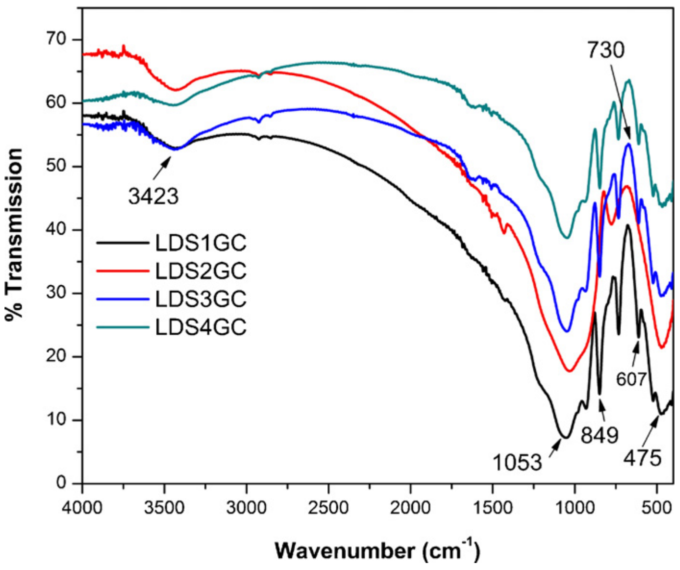

Fig. 5. FT-IR patterns of lithium disilicate glass–ceramics heat-treated at 700 °C for 1 h.

3.4. FT-IR spectroscopy

Fourier transform infrared spectroscopy (FT-IR) was used in order to obtain more structural information on the glass ceramics. The FT-IR transmittance spectra of the LDS glass–ceramics samples, LDS1GC, LDS2GC, LDS3GC and LDS4GC in the wavenumber range 400–4000 cm^{-1} are shown in Fig. 5. The IR spectra of glass–ceramics have their most prominent bands at 475, 607, 730, 849 and 1053 cm^{-1} and a weak band is observed at 518 cm^{-1}. This weak band at 518 cm^{-1} is assigned to Si–O deformation. The bands at 607 and 730 cm^{-1} are assigned to symmetric stretch of Si–O–Si vibrations. The band at 849 cm^{-1} is attributed to asymmetric Si–O–Si band or –O–Si–O– asymmetric vibrations found in crystalline LDS. The band at 3423 cm^{-1} is assigned to O–H stretching vibrations. The analysis of the results also reveals that with an increase in MnO_2 content in the glass, this Si–O–Si band intensity is reduced systematically. This is in good agreement with the results already reported by Fuss et al. [18].

3.5. Electron paramagnetic resonance studies

Fig. 6(a) shows the EPR spectra of Mn^{2+} ions in lithium disilicate glasses for different concentrations of manganese ions. The EPR spectrum of all the glass samples exhibit an intense resonance signal with effective g values at $g \approx 1.98$, a broad signal at $g \approx 3.3$ and weak shoulders at $g \cong 4.10$ and $g \approx 4.73$. At lower concentration of manganese (up to 1 wt%) the resonance signal at $g \approx 1.98$ exhibits a six line hyperfine structure (hfs) which is a characteristic of Mn^{2+} ions with a nuclear spin $I = 5/2$. Lithium disilicate glass ceramic samples were obtained by calcining the samples at 700 °C for 1 h. The EPR spectra of Mn^{2+} ions in lithium disilicate glass ceramic samples for different concentrations of manganese ions are shown in Fig. 6(b). It is observed that in ceramized samples, the hyperfine structure weakens or disappears even for lower concentration of manganese. Further, the signal intensity of the ceramized sample is greater than for the glass sample.

The presence of the resolved hyperfine structure (hfs) of the $g \approx 1.98$, resonance strongly indicates that Mn^{2+} ions in symmetric sites (octahedral) are isolated or significantly distinct from each other. As the concentration of Mn^{2+} ion increases beyond 1 mol%, the resolution of the hfs sextet disappears giving a single broad band. The resolution was lost with increased concentration due to the ligand field fluctuations near the Mn^{2+} ions and to the dipolar interactions. In general, Mn^{2+} ions in borate glass exist in octahedral coordination whereas in silicate and germanate glasses the Mn^{2+} ions exist in both octahedral and tetrahedral coordination [26]. In the case of d^5 transition metal ions, it is known that axial distortion of octahedral symmetry gives rise to three Kramers doublets $|\pm 5/2>$, $|\pm 3/2>$ and $|\pm 1/2>$ [27]. Application of the Zeeman field lifts the spin degeneracy of the Kramers doublets. As the crystal field splitting is normally much smaller than the Zeeman field, the resonances observed are due to transitions within the Zeeman field split Kramers doublets. The $g \approx 1.98$ resonance is due to the Mn^{2+} ions in an environment close to octahedral symmetry and is known to arise from the transition between the energy levels of the lower doublet. The resonance signals at $g \approx 3.3$ and $g \approx 4.05$ have been attributed to the rhombic symmetry of Mn^{2+} ions [28].

Van Wieringen [29] noted that the strength of the hyperfine splitting depends on the matrix into which the ion is dissolved and is mainly determined by the electronegativity of the neighbours. This means a qualitative measure of the covalency of the bonding in the matrix can be determined from the value of the hyperfine splitting constant A; smaller the value of A, the more the covalent the bonding of the anion. The magnitude of the hyperfine splitting constant, A_{avg} was measured using the expression:

$$A_{\mathrm{avg}} = \frac{(\Delta_{\mathrm{Opp}} + \Delta_{\mathrm{Ott}})/5 + (\Delta_{\mathrm{Mpp}} + \Delta_{\mathrm{Mtt}})/3 + (\Delta_{\mathrm{Ipp}} + \Delta_{\mathrm{Itt}})}{6} \tag{3}$$

where Δ_{Opp} and Δ_{Ott} represent the differences between the first and sixth peak positions, measured peak to peak and trough to trough, respectively. Δ_{Mpp} and Δ_{Mtt} represent difference in positions between second and fifth peaks, Δ_{Ipp} and Δ_{Itt} between second and third peaks. In the present work, the evaluated hyperfine (hf) splitting constant (A) is found to be 90 G which indicates that the bonding between Mn^{2+} ions and the neighbouring ligands is ionic [29,30].

The population difference between Zeeman levels (N) can be calculated by comparing the area under the absorption curve with that of a standard ($CuSO_4 \cdot 5H_2O$ in this study) of known concentration. Weil et al. [31] gave the following expression, which includes the experimental parameters of both sample and standard:

$$N = \frac{A_x(Scan_x)^2 G_{std}(B_m)_{std}(g_{std})^2[S(S+1)]_{std}(P_{std})^{1/2}}{A_{std}(Scan_{std})^2 G_x(B_m)_x(g_x)^2[S(S+1)]_x(P_x)^{1/2}}[Std] \tag{4}$$

where A is the area under the absorption curve which can be obtained by a double integration of the first derivative EPR absorption curve, *scan* is the magnetic field corresponding to a unit length of the chart, G is the gain, B_m is the modulation field width, g is the g factor, S is the spin of the system in its ground state. P is the power of the microwave. The subscripts '*x*' and '*std*' represent the corresponding quantities for Mn^{2+} glass/glass ceramic sample and the reference ($CuSO_4 \cdot 5H_2O$), respectively. The population difference between Zeeman levels (N) for lithium disilicate glasses and glass ceramic samples for $g \approx 1.98$ resonance is listed in Table 3. It is observed that N increases in glass samples as the concentration of manganese increases suggesting that most Mn^{2+} ions enter as paramagnetic species.

The EPR data can be used to calculate the paramagnetic susceptibility of the sample using the formula [32]:

$$\chi = \frac{Ng^2\beta^2 J(J+1)}{3k_B T} \tag{5}$$

where N is the number of spins per m^3 and the other symbols have their usual meaning. N can be calculated from Eq. (4). Since the intensity of the resonance signal at $g \approx 1.98$ is high, this g value is taken to calculate the paramagnetic susceptibility. The

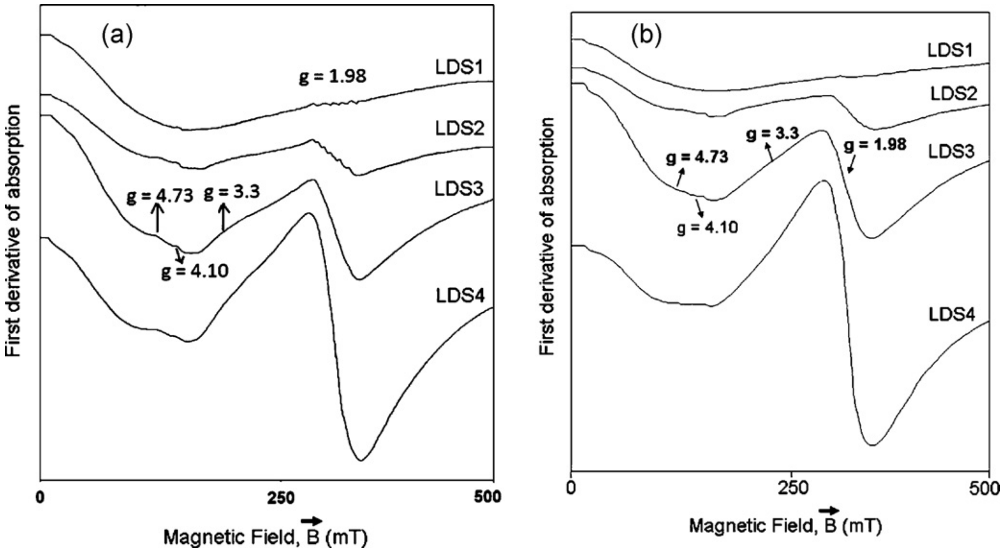

Fig. 6. EPR spectra of Mn^{2+} ions lithium disilicate (a) glass and (b) glass ceramics.

paramagnetic susceptibilities (χ) evaluated from EPR data are also presented in Table 3.

3.6. Optical studies

Fig. 7(a) shows the optical absorption spectrum of Mn^{2+} ions in LDS glasses and Fig. 7(b) that of glass–ceramic samples with different concentrations of manganese ions. In LDS glasses, the optical absorption spectrum exhibits a single broad band centered at 470 nm (20,320 cm^{-1}). In a octahedral crystalline field of low to moderate strength, the five d electrons of Mn^{2+} ions are distributed in the t_{2g} and e_g orbitals, with three in the former and two in the latter. Thus the ground state configuration is $(t_{2g})^3$ $(e_g)^2$. This configuration gives rise to the electronic states, $^6A_{1g}$, $^4A_{1g}$, ^4E_g, $^4T_{1g}$, $^4T_{2g}$ and to a number of doublet states of which $^6A_{1g}$ lies lowest according to Hund's rule. Since, all the excited states of Mn^{2+} ion (belonging to d^5 configuration) will be either quartets or doublets, the optical absorption spectra of Mn^{2+} ions will have only spin forbidden transitions. In the present case, the broad band observed near ~20,320 cm^{-1} is assigned to the transition $^6A_{1g}(S) \rightarrow {}^4A_{1g}(G)\ {}^4E_g(G)$. It is interesting to observe that in LDS glasses the transition $^6A_{1g}(S) \rightarrow {}^4A_{1g}(G)\ {}^4E_g(G)$ disappears. To confirm this the authors studied the photoluminescence spectra of Mn^{2+} ions in LDS glass ceramics. The excitation and emission spectra of Mn^{2+} ions in LDS glass ceramics are shown in Fig. 8(a) and (b), respectively. In the present study the excitation spectrum (Fig. 8(a)) shows 3 bands at 344 nm, 394 nm and 472 nm. Among these the 394 nm (25,380 cm^{-1}) band is the intense one. These bands arise due to the d–d transitions within the Mn^{2+} ($3d^5$) configuration from the ground state $^6A_1(S)$ of Mn^{2+} ions to various excited states. The emission at 565 nm (17,700 cm^{-1}) is the typical green emission. The emission process from this material is attributed to a d-level spin-forbidden transition for the Mn^{2+} ions acting as an activating center [33]. In particular, the transition from the lowest excited state to the ground state, $^4T_{1g}$ to $^6A_{1g}$, is directly responsible for the green light emission. Upon ceramization, the local environment of the transition metal ion incorporated into the glass leads to ligand field changes which may be reflected in the optical absorption and EPR spectra. Manganese ions emission wavelengths range from green to red; the green emission is characteristic of Mn^{2+} in tetrahedral coordination, and the orange to red colours come from octahedrally coordinated Mn^{2+}, with intermediate colours from a combination of both species [34]. An emission at 710 nm in the longer wavelength region is observed which might be due to the charge-transfer de-excitation associated with the Mn ion. The '*A*' value is one of the parameters to indicate the coordination number of Mn^{2+} ions which depends on the host matrix. The hyperfine splitting constant '*A*' value obtained in the present work (90 G) is similar to the values reported for octahedrally coordinated Mn^{2+} ions [34] and this suggests that the Mn^{2+} ions are in octahedral symmetry.

The refractive indices at standard wavelengths n'_F (480 nm), n_e (546.1 nm) and n'_C (643.8 nm) have been obtained from the dispersion curves by fitting the measured refractive indices with a five term Sellmeier equation [35]:

$$n^2 = A + \frac{B\lambda^2}{\lambda^2 - C} + \frac{D\lambda^2}{\lambda^2 - E} \tag{6}$$

where n is the refractive index at wavelength λ. Table 2 lists some important optical properties such as refractive index, Abbe number, reflection loss for the LDS glass and glass–ceramic samples studied.

Table 3
Number of spins (N), paramagnetic susceptibilities (χ) and optical band gap (E_{opt}) energies for the lithium disilicate glass and glass ceramic samples studied in the present work.

Sample	Number of Spins per kg × 10^{22} (arb. units)	Paramagnetic susceptibility × 10^{-3} m^3 kg^{-1}	Optical band gap energy E_{opt} (eV)
LDS1G	1.45	3.46	3.38
LDS2G	1.83	4.37	3.36
LDS3G	4.00	9.56	3.34
LDS4G	38.00	90.70	3.33
LDS1GC	2.41	5.76	1.82
LDS2GC	4.68	11.18	1.69
LDS3GC	5.99	14.31	1.54
LDS4GC	57.10	136.30	1.26

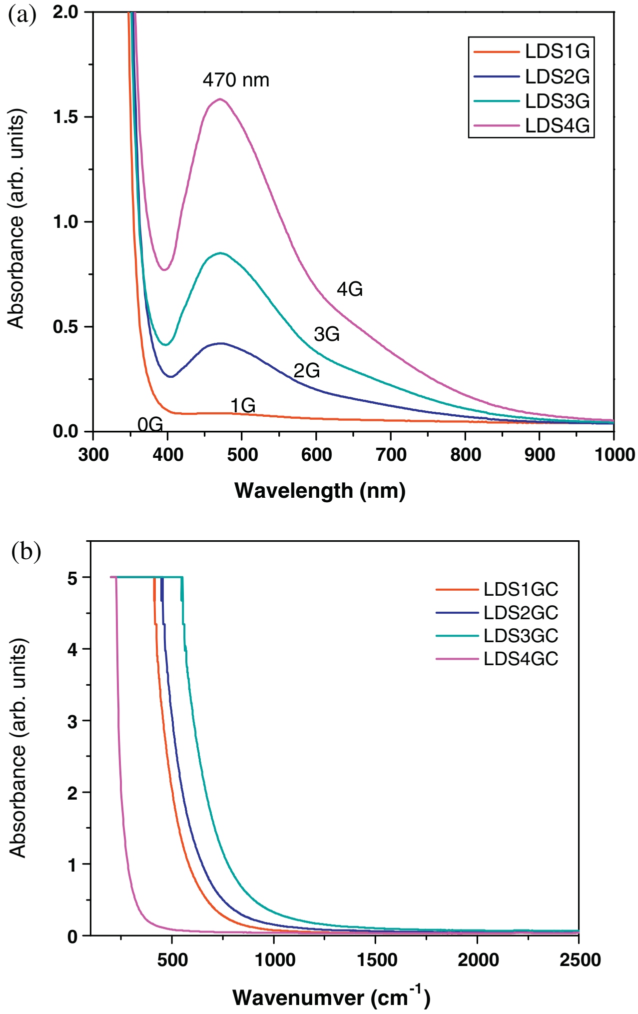

Fig. 7. Optical absorption spectra Mn^{2+} ions in (a) lithium disilicate glass and (b) glass ceramic samples at room temperature.

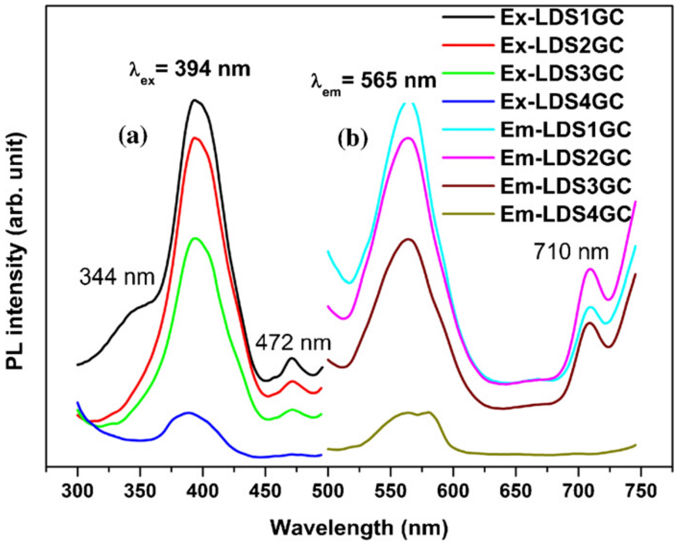

Fig. 8. Photoluminescence spectra of Mn^{2+} ions in LDS glass ceramics (a) excitation spectra (λ_{em} = 565 nm) and (b) emission spectra (λ_{ex} = 394 nm).

It will be interesting to observe, if there is any shift in the band gap in lithium disilicate glasses and glass–ceramics. In order to examine the optical band gap energy for the LDS glasses and glass ceramics, the optical absorption spectra were also recorded in the near ultra-violet region. The main feature of the absorption edge of amorphous semiconductors, particularly at the lower values of the absorption coefficient, is an exponential increase of the absorption coefficient $\alpha(\nu)$ with photon energy $h\nu$ in accordance with an empirical relation [36]:

$$\alpha = \alpha_0 \exp\left(\frac{h\nu}{\Delta E}\right) \tag{7}$$

where α_0 is a constant, ΔE is the Urbach energy and ν is the frequency of radiation.

The absorption coefficient $\alpha(\nu)$ can be determined near the edge using the formula:

$$\alpha(\nu) = \frac{2.303A}{d} \tag{8}$$

where 'A' is the absorbance at frequency ν and d is the thickness of the glass/glass ceramic sample. The optical band gap energy for an indirect transition can be determined using the formula [37]:

$$E_{\mathrm{opt}} = h\nu - \left(\frac{\alpha h\nu}{B}\right)^{1/2} \tag{9}$$

where 'B' is a constant and E_{opt} is the optical band gap energy. This relation is applied to many oxide glasses [36]. Figs. 9 and 10 show the plots between $(\alpha h\nu)^{1/2}$ and $h\nu$ for the LDS glass and glass ceramic, respectively. The optical band gap energy is determined by extrapolating the linear region of the curve to the $h\nu$ axis. The optical band gap energies obtained for the lithium disilicate glass and glass ceramics studied in the present work are listed in Table 3. From Table 3, the optical band gap energy is found to decrease slightly with the increase of concentration. The optical band gap energies obtained in the present work are of the same order as reported in the literature [38,39]. It is observed that in LDS glass ceramics there is a huge decrease in the optical band gap energies. The decrease in optical band gap energies can be attributed to the increase in non-bridging oxygen with the increase in Mn content.

3.7. *Mechanical properties*

The mechanical properties, i.e. hardness, indentation fracture toughness, 3-point flexural strength and elastic modulus of the LDS glass–ceramics have been evaluated and are presented in Table 4. The hardness of the heat-treated glass ceramic samples is measured by acquiring micro-indentation with a Vicker's indenter at an indent load of 500 g using the average diagonal lengths of the hardness impressions. Representative images of the indentation impressions of four varieties of LDS glass–ceramics samples observed under optical microscope are shown in Fig. 11. The maximum hardness value obtained (5.8) was for LDS1GC. For the other samples, the hardness values found were 5.4, 5.6 and 5.7, for LDS2GC, LDS3GC and LDS4GC respectively. No definite trend of hardness values could be established with increasing in MnO_2 content in the glass–ceramics but overall variations in hardness values are marginal. The hardness values of LDS glass–ceramics are more than for many other glasses and glass–ceramics [40]. This is primarily because the greater interlocking of the LDS nanocrystals in the glass–ceramic helps to stop the cracks more effectively, thereby enhancing the plastic deformation of the material.

Indentation fracture toughness values were calculated by measuring the average lengths of the cracks using Antis's equation [24]. Antis's equation used for the calculation of indentation fracture toughness yields reliable values of the fracture toughness, if

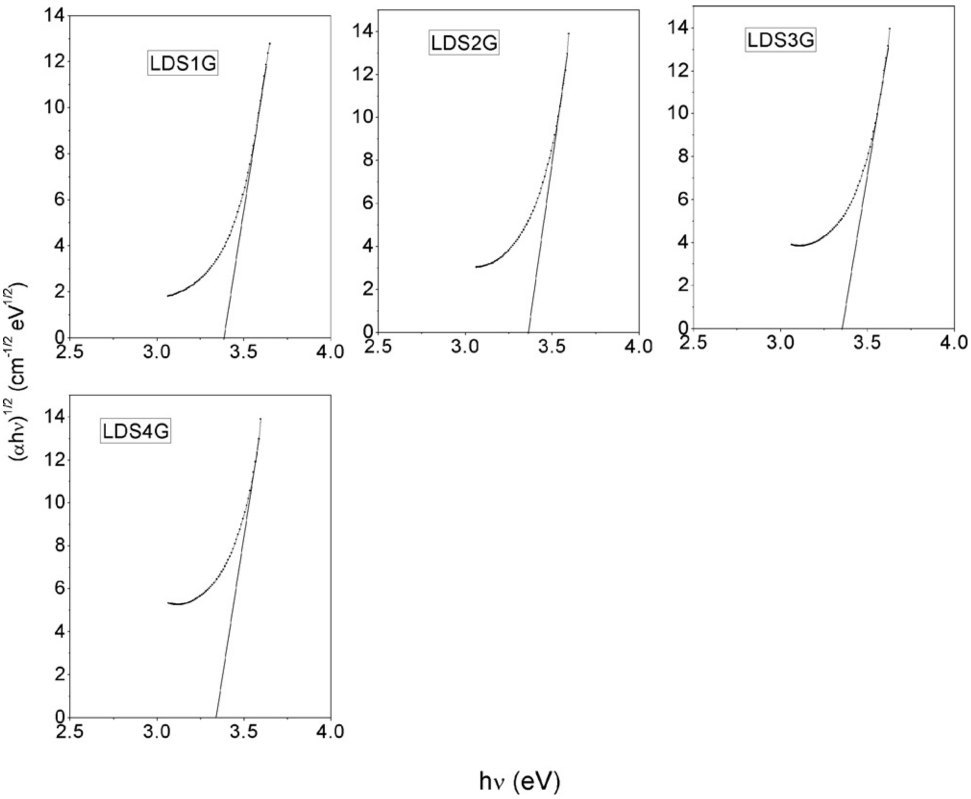

Fig. 9. Plots corresponding $(\alpha h\nu)^{1/2}$ vs. $h\nu$ for the lithium disilicate glasses at room temperature.

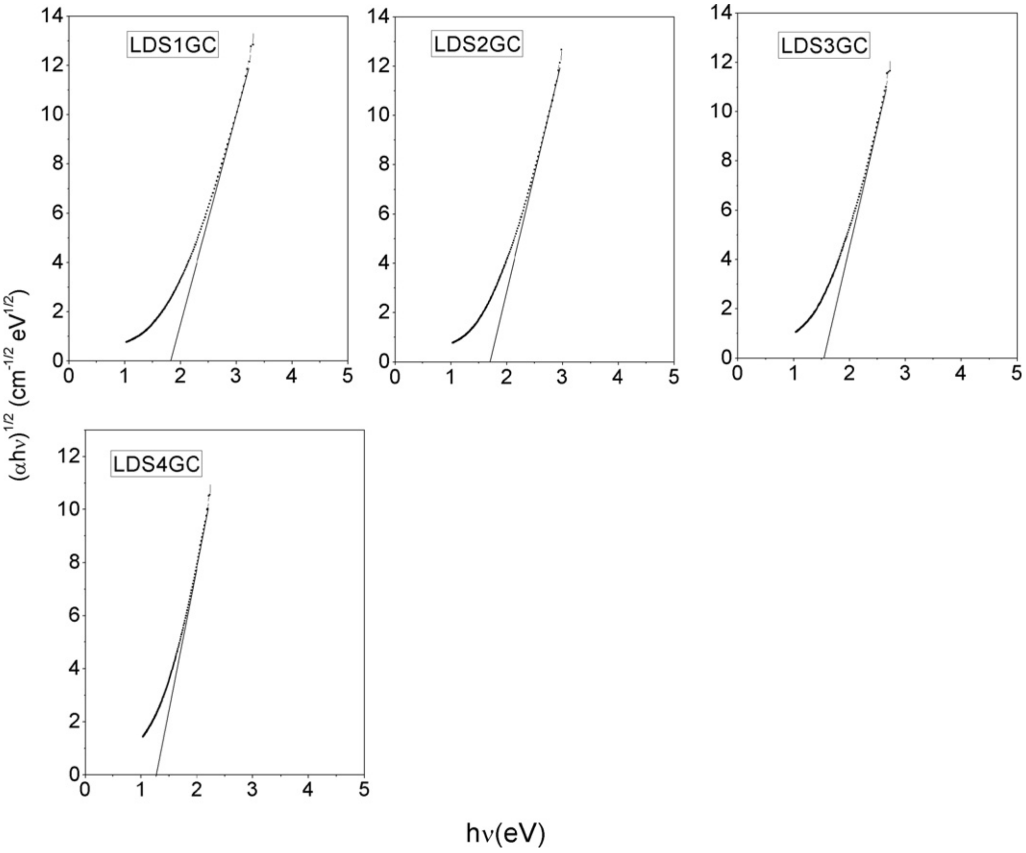

Fig. 10. Plots corresponding to $(\alpha h\nu)^{1/2}$ vs. $h\nu$ for the lithium disilicate glass ceramics at room temperature.

Table 4
Mechanical properties of lithium disilicate glass–ceramics heat-treated at 700 °C for 1 h.

Sample	Flexural strength (MPa)	*E*-modulus (GPa)	Hardness (GPa)	Crack length, *C* (μm)	Half diagonal length, *a* (μm)	*C*/*a*	Indentation fracture toughness (MPa m$^{1/2}$)
LDS1GC	241.9	73.78	5.8	96.13	40.2	2.39	2.63
LDS2GC	263.96	67.88	5.4	94.55	41.18	2.29	2.93
LDS3GC	226.13	65.54	5.6	94.40	40.3	2.33	2.78
LDS4GC	259.73	67.71	5.7	92.85	39.97	2.32	2.82

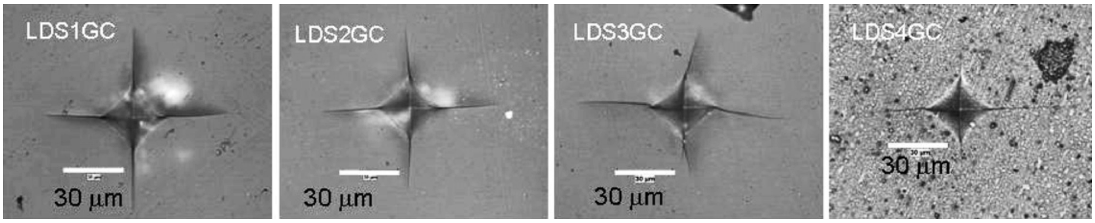

Fig. 11. Representative images of the indentation impressions of four varieties of LDS glass–ceramics samples observed under optical microscope (load used 500 g).

C/*a* < 2.5 (i.e. if the crack system is Palmquist type) where *C* is the average of half of the radian crack lengths and *a* is the average of half of the diagonal lengths of indentation impressions. *C*/*a* ratio have been measured for these LDS glass–ceramics and the values found to be in the range of 2.29–2.39 which is <2.5 even at higher loads of 500 g. Palmquist type radian cracks other researchers have also used Antis's equation [41] for calculating indentation fracture toughness. This equation is based on the assumption that nucleation of the cracks is due to an elastic stress field formed beneath the indenter when the indentations were taken. Though crack growth in elastic/plastic contact fields has been established as the basis for fracture studies, there is still sometimes a dominant residual component of the driving force which leads to an increase in the crack length even after completion of the actual indentation process [42]. Moreover, sometimes it has been observed that during indentation no cracks were visible in the sample in a particular direction, but after few seconds or so cracks started to appear. This is due to residual component of the driving force which leads to the formation of these cracks even after the indentation process is over. Particularly, for the LDS3GC and LDS4GC glass–ceramic samples, a black circle surrounding the indentation impressions were observed.

Indentation fracture toughness values of 2.63, 2.93, 2.78 and 2.82 MPa m$^{1/2}$ have been observed for the samples, LDS1GC, LDS2GC, LDS3GC and LDS4GC, respectively. Marginal variation in fracture toughness values are noticed due to the absence of any significant compositional difference between the samples. However, the indentation fracture toughness values observed in LDS glass–ceramics are higher than for other conventional glasses and glass ceramics.

The basic mechanical properties, i.e. flexural strength (3-point) and *E*-modulus of samples (LDS1GC, LDS2GC, LDS3GC and LDS4GC) were determined. The experimental results reveal that higher strength values of 242, 264, 226 and 260 MPa respectively could be obtained and also demonstrate moderate E-modulus values of 74, 68, 66 and 68 GPa respectively. In many of the published research articles on glass–ceramics, such comprehensive measurements of basic mechanical properties are not presented. This combination of enhanced strength and elastic modulus is attributed to the highly dense nano-crystals of LDS oriented in interlocking fashion in the glassy matrix.

Due to their high hardness, moderate fracture toughness along with enhanced flexural strength and elastic modulus, LDS glass–ceramics are widely used in the various biomedical applications. Very recently, transparent varieties of LDS glass–ceramics are getting huge attention for transparent armour applications due to their good mechanical properties, transparency and more importantly lightweight (2.5 g cm^{-3}) compared to their ceramic (~4 g cm^{-3}) counterparts.

4. Conclusions

By employing controlled crystallization heat-treatment in LDS glasses, it was possible to have a tight control over the crystallite size to the extent that the transparency of the host glass is retained. XRD results confirm that LDS was the only crystalline phase identified in all these glass–ceramics. The glass–ceramics are transparent due to the development of nano-sized crystals (~100 nm) and the crystals have an elongated, highly dense and interlocked microstructure. TEM images also reveal the presence of nanocrystals of average size of 10–50 nm. FT-IR results show symmetric stretch of Si–O–Si vibrations and –O–Si–O– asymmetric vibrations in crystalline LDS. The EPR spectrum exhibits resonance signals characteristic of Mn^{2+} ions. The resonance at $g \approx 1.98$ is due to the Mn^{2+} ions in an environment close to octahedral symmetry whereas the resonances at $g \approx 3.3$ and $g \approx 4.05$ have been attributed to Mn^{2+} ions in rhombic symmetry. The optical absorption spectrum of LDS glass shows a broad band at 20,320 cm^{-1} which is assigned to the transition $^6A_{1g}(S) \rightarrow {}^4T_{1g}(G)\ {}^4E_g(G)$. The emission at 565 nm (17,700 cm^{-1}) is the typical green emission attributed to a d–d level spin-forbidden transition for the Mn^{2+} ions from the lowest excited state to the ground state, $^4T_{1g}$ to $^6A_{1g}$. Upon ceramization, the local environment of the transition metal ion incorporated into the glass changes and leads to ligand field changes which are reflected in the optical absorption and EPR spectra. An emission at 710 nm in the longer wavelength region is observed which is due to the charge-transfer de-excitation associated with the Mn ion. In lithium disilicate glass ceramics there is a huge decrease in the optical band gap. The decrease in optical band gap can be attributed to an increase in non-bridging oxygens with an increase in Mn content. In the present study, a good combination of mechanical properties has been obtained including a micro-hardness of about ~5.6 GPa, high indentation fracture toughness ~2.8 MPa m$^{1/2}$, 3-point flexural strength of about ~250 MPa and moderate elastic modulus of about 65 GPa.

Acknowledgements

The authors gratefully acknowledge the support provided by Prof. I. Manna, Director of the Institute for carrying out this work.

Thanks are due to the CSIR, Government of India for their financial support (NWP 0029) for carrying out this investigation. Thanks are also due to the Electron Microscopy, XRD and Mechanical Characterization Sections of CSIR-CGCRI for their help in analyzing samples. Last but not the least, we gratefully acknowledge the efforts of Prof. J.M. Parker of The University of Sheffield, U K for improving the English as well as overall quality of the paper.

References

[1] W. Höland, G. Beall, Glass–Ceramic Technology, The American Ceramic Society, Westerville, OH, 2002.
[2] E. Apel, C. van't Hoen, V. Rheinberger, W. Höland, J. Eur. Ceram. Soc. 27 (2007) 1571.
[3] W. Höland, M. Schweiger, M. Frank, V. Rheinberger, J. Biomed. Mater. Res. (Appl. Biomater.) 53 (2000) 297.
[4] T.B. da Cunha, J.P. Wu, O. Peitl, V.M. Fokin, E.D. Zanotto, L. Iannucci, A.R. Boccaccini, Adv. Eng. Mater. 9 (2007) 191.
[5] M. Schweiger, W. Höland, M. Frank, H. Drescher, V. Rheinberger, Quint. Dent. Technol. 22 (1999) 143.
[6] D. John, Patent no. WO 03/022767 A1 (2003).
[7] H. Fischer, R.A. De Souza, A.M. Wätjen, S. Richter, D. Edelhoff, J. Mayer, M. Martin, R. Telle, J. Biomed. Mater. Res. 87A (2008) 582.
[8] F.H. Batal, M.A. Azooz, Y.M. Hamdy, Ceram. Int. 35 (2009) 1211–1218.
[9] J. Cheng, D. Xiong, H. Li, H. Wang, J. Alloys Compd. 507 (2010) 531.
[10] S.C. von Clausbruch, M. Schweiger, W. Höland, V. Rheinberger, J. Non-Cryst. Solids 263&264 (2000) 388–394.
[11] G. Wen, X. Zheng, L. Song, Acta Mater. 55 (2007) 3583–3591.
[12] X. Zheng, G. Wen, L. Song, X.X. Huang, Acta Mater. 56 (2008) 549–558.
[13] M. Bengisu, R.K. Brow, J. Non-Cryst. Solids 331 (2003) 137–144.
[14] L.L. Burgner, M.C. Weinberg, P. Lucas, P.C. Soares Jr., E.D. Zanotto, J. Non-Cryst. Solids 255 (1999) 264–268.
[15] L.L. Burgner, P. Lucas, M.C. Weinberg, P.C. Soares Jr., E.D. Zanotto, J. Non-Cryst. Solids 274 (2000) 188–194.
[16] D. Xiong, J. Cheng, H. Li, J. Alloys Compd. 498 (2010) 162.
[17] V.M. Fokin, E.D. Zanotto, J.W.P. Schmelzer, O.V. Potapov, J. Non-Cryst. Solids 351 (2005) 1491.
[18] T. Fuss, A. Mogus-Milankovic, C.S. Ray, C.E. Lesher, R. Youngman, D.E. Day, J. Non-Cryst. Solids 352 (2006) 4101.
[19] T. Fuss, C.S. Ray, C.E. Lesher, D.E. Day, J. Non-Cryst. Solids 352 (2006) 2073.
[20] C. Bischoff, H. Eckert, E. Apel, V.M. Rheinberger, W. Höland, Phys. Chem. Chem. Phys. 13 (2011) 4540.
[21] Z. Khalkhali, B. Eftekhari yekta, V.K. Marghussian, Int. J. Appl. Ceram. Technol. (2011) 1–10, doi:10.1111/j.1744-7402.2011.02661.x.
[22] P. Goharian, A. Nemati, M. Shabanian, A. Afshar, J. Non-Cryst. Solids 356 (2010) 208.
[23] W. Höland, E. Apel, Ch. van‘t Hoen, V. Rheinberger, J. Non-Cryst. Solids 352 (2006) 4041.
[24] G.R. Antis, P. Chantikul, B.R. Lawn, D.B. Marshall, J. Am. Ceram. Soc. 64 (1981) 533.
[25] W. Höland, V. Rheinberger, E. Apel, C. Ritzberger, Phys. Chem. Glasses: Eur. J. Glass Sci. Technol. B 48 (2007) 97.
[26] A. Van Die, A.C.H.I. Leenaers, G. Blasse, W.F. Van Der Weg, J. Non-Cryst. Solids 99 (1988) 32.
[27] A. Abragam, B. Bleaney, Electron Paramagnetic Resonance of Transition Ions, Clarendon, Oxford, 1970.
[28] E.A. Harris, Phys. Chem. Glasses 28 (1987) 96.
[29] J.S. Van Wieringen, Discuss. Faraday Soc. 19 (1955) 118.
[30] P. Pascuta, M. Bosca, G. Borodi, E. Culea, J. Alloys Compd. 509 (2011) 4314.
[31] J.A. Weil, J.R. Bolton, J.E. Wertz, Electron Paramagnetic Resonance—Elementary Theory and Practical Applications, Wiley, New York, 1994, p. 498.
[32] N.W. Aschcroft, N.D. Mermin, Solid State Physics, Harcourt College Publishers, 2001, p. 656.
[33] C.R. Kesavulu, R.S. Muralidhara, J.L. Rao, R.V. Anavekar, R.P.S. Chakradhar, J. Alloys Compd. 486 (2011) 46.
[34] R.W.A. Franco, J.F. Lima, C.J. Magon, J.P. Donoso, Y. Messaddeq, J. Non-Cryst. Solids 352 (2006) 3414.
[35] A.D. Sontakke, K. Biswas, A.K. Mandal, K. Annapurna, Appl. Phys. B 101 (2010) 235.
[36] M.A. Hassan, C.A. Hogarth, J. Mater. Sci. 23 (1988) 2500.
[37] E.A. Davis, N.F. Mott, Philos. Mag. 22 (1970) 903.
[38] A. Murali, J.L. Rao, J. Phys.: Condens. Matter 11 (1999) 7921.
[39] A.A. Kutub, J. Mater. Sci. 23 (1988) 2495.
[40] A.R. Molla, B. Basu, J. Mater. Sci.: Mater. Med. 20 (2009) 869.
[41] V. Le Houerou, J.-C. Sangleboeuf, S. Deriano, T. Rouxel, G. Duisit, J. Non-Cryst. Solids 316 (2003) 54.
[42] K.K. Bamzai, P.N. Kotru, J. Mater. Sci. Technol. 16 (2000) 405.